

Magnetic field at a jet base: extreme Faraday rotation in 3C 273 revealed by ALMA

T. Hovatta^{1,5}, S. O'Sullivan², I. Martí-Vidal³, T. Savolainen^{4,5,6}, and A. Tchekhovskoy^{7,8}

¹ Tuorla Observatory, University of Turku, Väisäläntie 20, FI-21500 Piikkiö, Finland
e-mail: talvikki.hovatta@utu.fi

² Hamburger Sternwarte, Universität Hamburg, Gojenbergsweg 112, D-21029 Hamburg, Germany

³ Department of Earth and Space Sciences, Chalmers University of Technology, Onsala Space Observatory, SE-439 92, Onsala, Sweden

⁴ Aalto University Department of Electronics and Nanoengineering, PL 15500, FI-00076 Aalto, Finland

⁵ Aalto University Metsähovi Radio Observatory, Metsähovintie 114, FI-02540 Kylmälä, Finland

⁶ Max-Planck-Institut für Radioastronomie, Auf dem Hügel 69, D-53121 Bonn, Germany

⁷ Center for Interdisciplinary Exploration & Research in Astrophysics (CIERA), Physics & Astronomy, Northwestern University, Evanston, IL 60202, USA

⁸ Departments of Astronomy and Physics, Theoretical Astrophysics Center, University of California Berkeley, Berkeley, CA 94720-3411, USA

Received XXX accepted XXX

ABSTRACT

Aims. We have studied the polarization behavior of the quasar 3C 273 over the 1 mm wavelength band at ALMA with a total bandwidth of 7.5 GHz across 223 to 243 GHz at 0.8'' resolution, corresponding to 2.1 kpc at the distance of 3C 273. With these observations we are able to probe the optically thin polarized emission close to the jet base, and constrain the magnetic field structure at the jet launching region.

Methods. We compute the Faraday rotation measure using simple linear fitting and Faraday rotation measure synthesis. In addition, we model the broadband behavior of the fractional Stokes Q and U parameters (qu-fitting). The systematic uncertainties in the polarization observations at ALMA are assessed through Monte Carlo simulations.

Results. We find the unresolved core of 3C 273 to be 3.3% linearly polarized. We detect a very high rotation measure (RM) of $(3.6 \pm 0.3) \times 10^5 \text{ rad m}^{-2}$ over the 1 mm band with all the methods we have used. This results in a rotation of $> 30^\circ$ of the intrinsic electric vector position angle, which is significantly higher than typically assumed for millimeter wavelengths. Our qu-fitting results strongly favor depolarization models over an external Faraday screen without depolarization. For a single region dominating the polarized emission, the RM and depolarization we observe can be explained by external Faraday dispersion ($\sigma_{\text{RM}} \sim 2.7 \times 10^5 \text{ rad m}^{-2}$) or an ordered RM gradient ($\Delta\text{RM} \sim 8.7 \times 10^5 \text{ rad m}^{-2}$) within the synthesized beam. Further multifrequency and high angular resolution observations are needed to determine the location and structure of the magnetic field of the Faraday active region. Comparing our RM estimate with values obtained at lower frequencies, the RM increases as a function of observing frequency, following a power law with an index of 1.9 ± 0.2 , consistent with a sheath surrounding a conically expanding jet. We also detect $\sim 0.2\%$ circular polarization, although further observations are needed to confirm this result.

Key words. polarization – galaxies: jets – quasars: individual: 3C 273 – radio continuum: galaxies

1. Introduction

Magnetic fields are thought to play a significant role in the formation of relativistic jets in active galactic nuclei (AGN). Magnetic fields can extract energy from the spinning supermassive black hole via the Blandford-Znajek mechanism (Blandford & Znajek 1977), launching a magnetically dominated outflow. In recent years, a major leap forward has been achieved through general relativistic magnetohydrodynamic (GRMHD) simulations of black hole accretion that show how this process can efficiently launch jets (e.g., McKinney & Gammie 2004; De Villiers et al. 2005; Hawley & Krolik 2006; McKinney & Blandford 2009; Tchekhovskoy et al. 2011).

Polarization observations, especially observations of Faraday rotation, can be used to probe the magnetic fields and magnetized plasma around relativistic jets, providing means to connect observations to the theory of jet formation. When syn-

chrotron emission passes through magnetized plasma, it undergoes Faraday rotation due to an induced phase offset between the velocities of the orthogonal plasma modes (Burn 1966). The amount of Faraday rotation, the rotation measure (RM), is proportional to the electron density n_e of the plasma (in cm^{-3}) and the magnetic field component \mathbf{B} (in μG) along the line of sight (in parsecs), given by

$$\text{RM} = 0.81 \int n_e \mathbf{B} \cdot d\mathbf{l} \text{ rad m}^{-2}. \quad (1)$$

In the simplest case, Faraday rotation results in a linear dependence between the observed electric vector position angle (EVPA, χ_{obs}) and wavelength squared (λ^2) so that $\chi_{\text{obs}} = \chi_0 + \text{RM}\lambda^2$, where χ_0 is the intrinsic electric vector position angle of the emission region. This allows one to estimate the amount of Faraday rotation by observing the EVPA at multiple frequencies.

Centimeter-band Faraday rotation observations give us information about the magnetic field structure around the jets on parsec scales. The RM of the cores of AGN at cm-wavelengths are typically up to a few thousand rad m^{-2} (e.g. Taylor 1998; Hovatta et al. 2012), indicating magnetic field strengths of a few μG , if the Faraday rotating screen is the narrow line region of the source (Zavala & Taylor 2004). In order to study the plasma close to the black hole, millimeter-band observations are required to probe the jet base in the optically thin regime (e.g., Lobanov 1998). Plambeck et al. (2014) detected a high rotation measure of $9 \times 10^5 \text{ rad m}^{-2}$ in the radio galaxy 3C 84 using observations from SMA and CARMA. In the low-luminosity AGN M87, a high rotation measure of $\text{RM} < 2 \times 10^5 \text{ rad m}^{-2}$ was detected in the SMA observations by Kuo et al. (2014). These observations were interpreted by assuming that the Faraday rotation occurs in the radiatively inefficient accretion flow, and both studies estimated the mass accretion rate onto the black hole. Recently, Mościbrodzka et al. (2017) showed that in the case of M87, the polarized emission and Faraday rotation is most likely dominated by the forward jet instead of the accretion flow, which limits the use of the RM to probe the accretion rate even in the low-luminosity sources.

The highest RM detected so far, $2 \times 10^7 \text{ rad m}^{-2}$ ($\sim 10^8 \text{ rad m}^{-2}$ in the source frame), was seen in the high-power gravitationally lensed quasar PKS 1830–211 in dual-polarization ALMA observations by Martí-Vidal et al. (2015). Based on the frequency-dependence of the rotation measure, they argued that the Faraday rotation must originate in the jet from a region 0.01 parsec away from the black hole. Their result implies that the electron density and/or magnetic field is high, of the order of at least tens of Gauss, in the jet launching region.

In this paper, we present the first full polarization ALMA observations of the nearest high-power quasar 3C 273 ($z = 0.158$, Strauss et al. 1992) over the 1 mm wavelength range. We selected 3C 273 for our pilot study because earlier observations of it in the 7mm to 3mm range have shown indications of $|\text{RM}| > 2 \times 10^4 \text{ rad m}^{-2}$ (Attridge et al. 2005; Hada et al. 2016, Savolainen et al. in prep.), making it a good candidate for high-RM studies in the 1 mm band.

Our paper is organized as follows: The observations and data reduction are described in Sect. 2. Section 3 contains our Faraday rotation and polarization modeling results. We present our discussion in Sect. 4 and list our conclusions in Sect. 5. We define the spectral index α such that the total intensity I at frequency ν follows the relation $I_\nu \propto \nu^\alpha$.

2. ALMA observations and data reduction

The Cycle 4 ALMA observations at band 6 (1.3 mm) were taken on December 20, 2016 using 44 of the 12-m antennas. The observations lasted from 09:32 UTC until 12:05 UTC with a total integration time of about 73 min on 3C 273¹. Our observations were taken in full polarization mode using the recommended continuum setup for band 6, where the four 1.875 GHz spectral windows (spw), each consisting of 64 channels that are 31.25 MHz wide, are placed at 224, 226, 240, and 242 GHz. The total bandwidth in our observations was then 7.5 GHz. The angular resolution (size of the synthesized beam) was $0.8''$. 3C 279 was ob-

¹ A second observation to complete the 3 hour program was conducted on December 28, 2016, but the duration of track was only 72 minutes with insufficient parallactic angle coverage to calibrate the polarization, which is why these data are not used in the analysis.

served as a bandpass and polarization calibrator and J1224+0330 as the gain calibrator.

The data reduction was done using Common Astronomical Software Applications (CASA) version 4.7.0. The amplitude scale of the observations was set using 3C279, assuming a flux density of 5.86 Jy at 233 GHz with a spectral index of -0.63 . Instead of using J1224+0330 (estimated flux density of 0.35 Jy) to correct for the gain variations², we performed self-calibration on 3C 273 as it is much brighter (mean flux density of 4.5 Jy), and provides better solutions. Calibration of the cross-hand delay, cross-hand phase and instrumental polarization (D-terms) was done using 3C279. For details of the standard data reduction and polarization calibration steps, see Nagai et al. (2016).

In our analysis, we assume that the emission in 3C 273 is dominated by the central point source at the phase center of the image. In order to obtain Stokes parameters of each 31.25 MHz wide spectral channel, we use the external CASA library UV-MULTIFIT (Martí-Vidal et al. 2014) to fit the visibility data. We fit a centered delta component to each channel individually to obtain the Stokes I, Q, U, and V values. These are reported in Table 1 (available in the electronic version) along with the derived polarization fraction and EVPA.

Following Vlemmings et al. (2017), we perform Monte Carlo (MC) simulations to assess the uncertainties in the Stokes parameters. These simulations, accounting especially for the systematic calibration uncertainties, are described in detail in Appendix A. We find that the uncertainty is on average 2.5 mJy in Stokes I, 6.8 mJy in Stokes Q, and 2.3 mJy in Stokes U. This results in a high accuracy of $\sim 0.15\%$ in the fractional polarization, while the EVPA uncertainty is of the order of 0.5° . We report the standard deviation of the 100 MC simulations as the uncertainty for each parameter in Table 1.

3. Results

In this section we describe the methods to analyze the polarization data over the ALMA 1 mm band. Thanks to the wide ALMA bandwidth of 7.5 GHz spread over a wide frequency range from 223 GHz to 243 GHz, we are able to study the polarization over the single observing band. We first determine the RM using multiple methods and then model the Stokes I, Q and U behavior as a function of wavelength squared using the broadband polarization modeling technique known as qu-fitting (e.g., Farnsworth et al. 2011; O’Sullivan et al. 2012; Farnes et al. 2014; Anderson et al. 2016; O’Sullivan et al. 2017; Schnitzeler 2018). In addition to the RM, this method can provide an estimate of the depolarization in the Faraday medium.

3.1. RM determination

The simplest way to estimate the RM is to directly fit the EVPAs as a function of wavelength squared. The underlying assumption is that the RM is caused by a single external Faraday screen, which results in a linear relation between the EVPAs and wavelength squared. This fit is shown in Fig. 1, and from the slope we obtain an $\text{RM} = (+3.6 \pm 0.02) \times 10^5 \text{ rad m}^{-2}$. The intrinsic EVPA given by the intercept is 49° , meaning that the Faraday rotation has a significant effect on the observed EVPAs, unlike typically assumed at mm wavelengths.

While the advantage of this method is its simplicity, one needs to manually adjust for any possible $n\pi$ ambiguities in the

² In standard ALMA observations a gain calibrator is always included even if the target itself is bright.

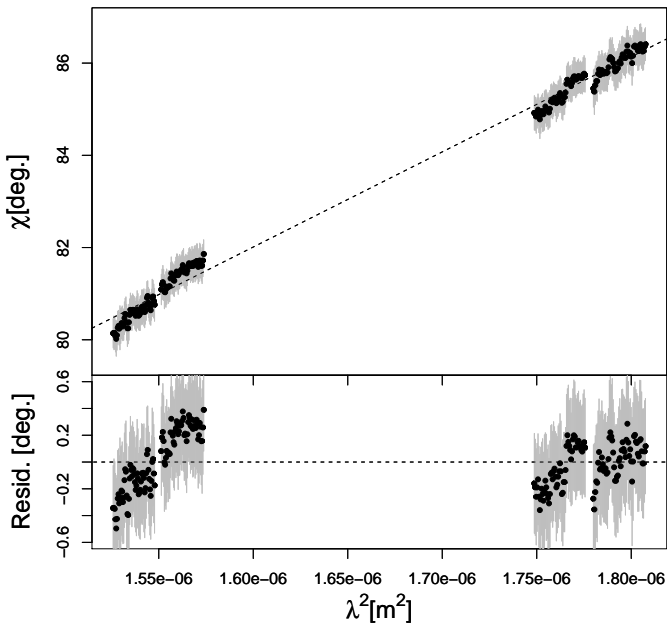


Fig. 1. Top: EVPAs as a function of wavelength squared for 3C 273 over the ALMA 1 mm band. The uncertainties in the EVPA are obtained through MC simulations described in Appendix A. The dashed line is a linear fit to the data giving $RM = (3.6 \pm 0.02) \times 10^5 \text{ rad m}^{-2}$ and intrinsic EVPA of 49° . Bottom: Residuals of the fit with MC uncertainties shown in gray.

EVPAs. Looking at the residuals in Fig. 1, one can see that all the spectral windows do not fall exactly on this line. This may indicate that the EVPAs do not follow a simple λ^2 -law and highlights that the simple method does not give correct results if there are multiple polarized components that undergo different amount of Faraday rotation. These problems can potentially be overcome by using Faraday rotation measure synthesis (Brentjens & de Bruyn 2005), where one coherently searches for polarized emission as a function of Faraday depth.

The nominal RM resolution of our observation is $\sim 1.3 \times 10^7 \text{ rad m}^{-2}$, estimated from the FWHM of the rotation measure spread function (RMSF).³ The maximum RM that can be measured from our data is $\sim \pm 4 \times 10^9 \text{ rad m}^{-2}$ and the maximum scale⁴ in RM is $\sim 2 \times 10^6 \text{ rad m}^{-2}$ (meaning that RM structures broader than this will be heavily depolarized). By applying RM synthesis to the full dataset, we find an RM of $(+3.59 \pm 0.05) \times 10^5 \text{ rad m}^{-2}$ with a degree of polarization of $(3.31 \pm 0.01)\%$ ($\sim 150 \text{ mJy beam}^{-1}$ at 233 GHz). We also apply RM CLEAN (Heald et al. 2009) to deconvolve the RM spectrum, but find no additional peaks in the RM spectrum significantly above the band-averaged noise level of $\sim 0.3 \text{ mJy beam}^{-1}$ (Figure 2).

Due to the excellent sensitivity, we could also achieve high signal to noise detections by running RM synthesis on the data from each of the four 1.875 GHz spectral windows, individually. In all cases, we find a higher RM with the values for spw0/spw1/spw2/spw3 corresponding to $5.1/6.6/5.0/5.7 \times 10^5 \text{ rad m}^{-2}$, respectively, with uncertainties of $\sim 10^4 \text{ rad m}^{-2}$. The difference between these values and the band-averaged RM

³ In practice, an RM smaller than this resolution can be identified at high signal to noise, analogous to determining the centroid of a radio source at higher precision than the nominal angular resolution.

⁴ Analogous to the largest angular scale of emission detectable by an interferometer.

may be related to underlying Faraday complexity, but we suspect it is more likely related to the calibration between spectral windows (for example, due to atmospheric lines not included in the MC simulations determining our uncertainties), and that the true RM is possibly as high as indicated by the individual spectral window RMs.

A third way to estimate the RM is through the qu-fitting technique (see the next section for details). This method gives $RM = (+3.6 \pm 0.2) \times 10^5 \text{ rad m}^{-2}$ if the RM is due to a turbulent external screen, and $RM = (+3.6 \pm 0.3) \times 10^5 \text{ rad m}^{-2}$ if the RM is due to a smooth gradient over the screen, which are fully consistent with the estimates by the simple linear fit and RM synthesis over the full bandwidth.

3.2. Polarization modeling

As described in Sect. 1, in the simplest case, the Faraday rotation is due to an external screen that does not cause depolarization. If the Faraday rotating medium is mixed with the emitting region, or if there are variations in the RM screen over the finite resolution of the observations, depolarization towards longer wavelengths may be seen (Burn 1966).

In order to investigate the Faraday depolarization properties of the data in a quantitative manner, we used the qu-fitting technique. We considered three different ‘single RM component’ models to fit the data: 1a. No depolarization, 1b. Depolarization due to random magnetic fields (σ_{RM}), and 1c. Depolarization due to ordered magnetic fields (ΔRM) (Sokoloff et al. 1998). The parameters and functional form of the three models are shown in Eqn. 2.

$$P = q + iu = p_0 e^{2i(\chi_0 + RM\lambda^2)} e^{-2\sigma_{RM}\lambda^4} \text{sinc } \Delta RM\lambda^2 \quad (2)$$

where, $q = Q/I$ and $u = U/I$. In Model 1a, we fit for p , RM , χ_0 with $\sigma_{RM} = \Delta RM = 0$. In Model 1b, we fit for p , RM , χ_0 and σ_{RM} , with $\Delta RM = 0$. In Model 1c, we fit for p , RM , χ_0 and ΔRM , with $\sigma_{RM} = 0$.

In order to estimate more realistic errors based on the expected calibration errors and not just the thermal noise, a Monte Carlo analysis was applied to the data (see Appendix A for details). The qu-fitting was then run on each of the Monte Carlo datasets (100 in total). The median best fitting parameters and model selection criteria are shown in Table 2 and example fits for each model are shown in Fig. 3. The quoted parameter errors are derived as the median absolute deviation from the median. The RM for all three models is consistent between the models and also consistent with the results from RM synthesis and the polarization angle fitting. The models with depolarization (Models 1b & 1c) are strongly favored by the Bayesian Information Criteria (BIC)⁵ over Model 1a, which has no depolarization ($BIC_{1a} - BIC_{1b} = 394$, $BIC_{1a} - BIC_{1c} = 375$). This gives us confidence that the depolarization we observe is real and not due to errors in the polarization calibration.

Formally, Model 1b is slightly favored over Model 1c ($BIC_3 - BIC_2 = 18$) suggesting that Faraday depolarization due to random magnetic fields (with $\sigma_{RM} = (2.7 \pm 0.1) \times 10^5 \text{ rad m}^{-2}$) is more likely than Faraday depolarization from ordered magnetic fields (with $\Delta RM = (8.7 \pm 0.6) \times 10^5 \text{ rad m}^{-2}$). Two physical scenarios for the origin of this depolarization could be either turbulent magnetic fields in the accretion disk or accretion disk wind (Mościbrodzka et al. 2017) or uniform magnetic fields

⁵ The model with the lowest BIC value is preferred (c.f. Raftery 1995).

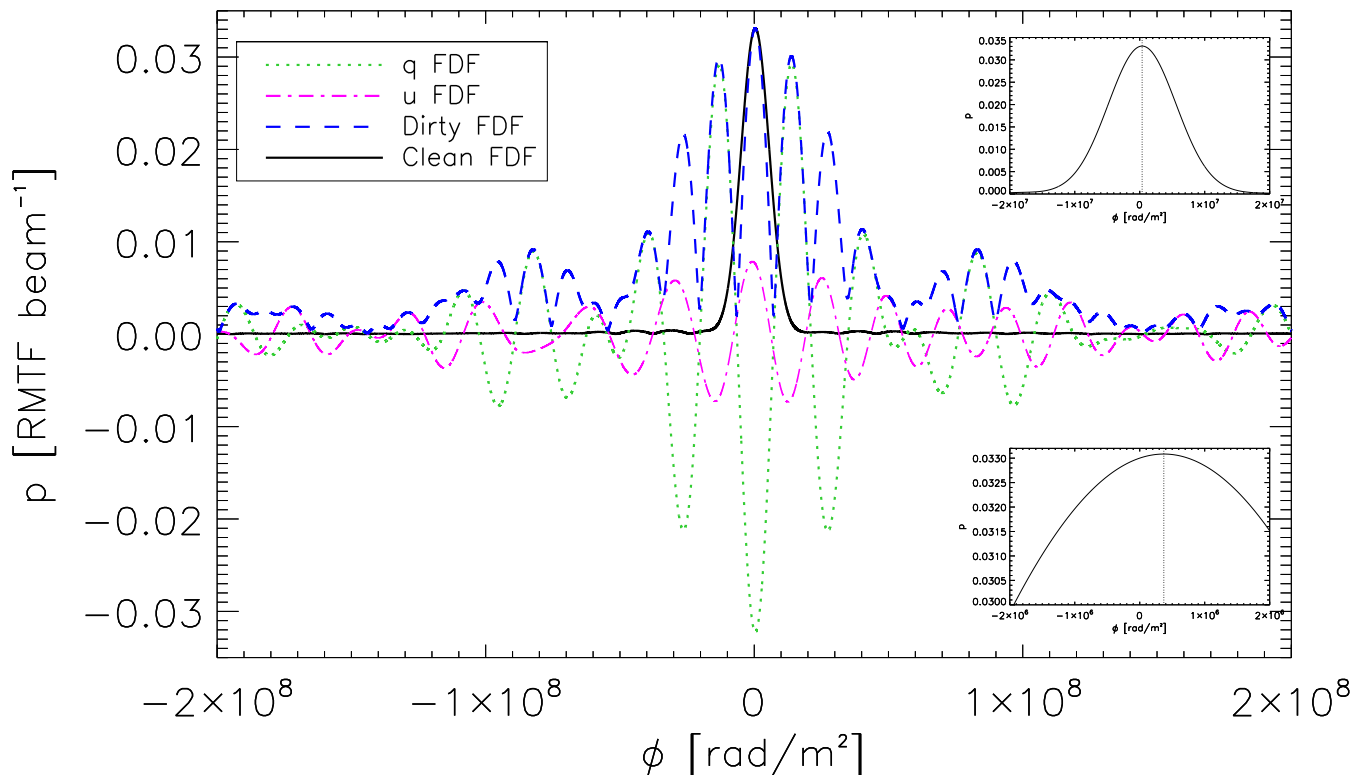


Fig. 2. Amplitude of the Faraday dispersion function (FDF) after applying RM synthesis. The Faraday depth (ϕ) varies from -2×10^8 to $+2 \times 10^8$ rad m^{-2} sampled at intervals of 10^4 rad m^{-2} . The dirty FDFs are shown for $q = Q/I$ (green-dotted line), $u = U/I$ (magenta-dot-dashed line), and p (blue-dashed line), while the FDF after applying RM CLEAN is shown as the solid black line. The inset in the top-right is a zoom-in of the main lobe of the FDF, while the bottom-right is further zoomed-in to highlight the non-zero Faraday depth of the peak polarized emission (vertical dotted line in both cases).

Table 2. Median best-fitting parameters from qu-fitting on the 100 Monte-Carlo realisations.

Model	RM	σ_{RM}	ΔRM	p_0	χ_0	BIC
1a	+3.60(4)	–	–	3.31(1)	50(2)	–4380
1b	+3.6(2)	2.7(1)	–	5.0(2)	45(6)	–4774
1c	+3.6(3)	–	8.7(6)	4.8(3)	47(7)	–4755

RM, σ_{RM} and ΔRM in units of 10^5 rad m^{-2} . p_0 in per cent and χ_0 in degrees.

close to the jet boundary that are expected to produce the transverse RM gradients observed at lower frequencies (e.g., Broderick & McKinney 2010). However, our current wavelength-squared coverage is not sufficient to uniquely distinguish between these two possibilities, or to determine if there is a partial contribution from both random and ordered magnetic field components.

If we extend Model 1b & 1c in wavelength-squared to include ALMA Band 4, then Model 1b predicts less than 0.2% polarization, while in Model 1c the degree of polarization is ~ 0.8 to 1%. This highlights the ability of the lower frequency ALMA bands to potentially distinguish between Faraday depolarization models.

4. Discussion

In the previous section we have shown that we detect a Faraday rotation measure of $\text{RM}_{\text{obs}} \sim +3.6 \times 10^5$ rad m^{-2} in 3C 273

over the 1 mm-band (224 – 242 GHz) of ALMA. Recently, Bower et al. (2017) reported 1 mm RM observations of the low-luminosity galaxies M81 and M84 obtained at SMA and CARMA. In their SMA observations, 3C 273 was used as a calibrator, and they report a value of RM consistent with zero in their observations. However, they only used a bandwidth of 4 GHz in the RM calculation, which is not wide enough to reveal an RM of $+3.6 \times 10^5$ rad m^{-2} because of their larger uncertainties.

The value we obtain is about an order of magnitude higher than $|\text{RM}| > 2 \times 10^4$ rad m^{-2} , reported for 3C 273 in observations between 3 mm and 7 mm (Attridge et al. 2005; Hada et al. 2016, Savolainen et al. in prep.), suggesting a denser Faraday screen or a higher magnetic field strength over the 1 mm emission region. Savolainen et al. (2008) estimated the magnetic field strength as a function of distance from the jet apex in 3C 273 using multi-frequency Very Long Baseline Interferometry (VLBI) observations. They found the magnetic field to be ~ 2 G in their 3 mm core, at a distance of ≤ 0.06 mas from the jet apex. Assuming that the jet is conical and that the magnetic field follows the relation $B \propto r^{-1}$ as expected for the toroidal component of the field (which could be expected to correspond to the line-of-sight component of the field), we would expect the magnetic field strength to be about 6 G in our observations. Using Eq. 1 we can then estimate the electron density in the Faraday rotating medium. If the path length through the medium is 1 pc, we obtain $n_e = 7.4 \times 10^{-2} \text{cm}^{-3}$, which is close to the central density

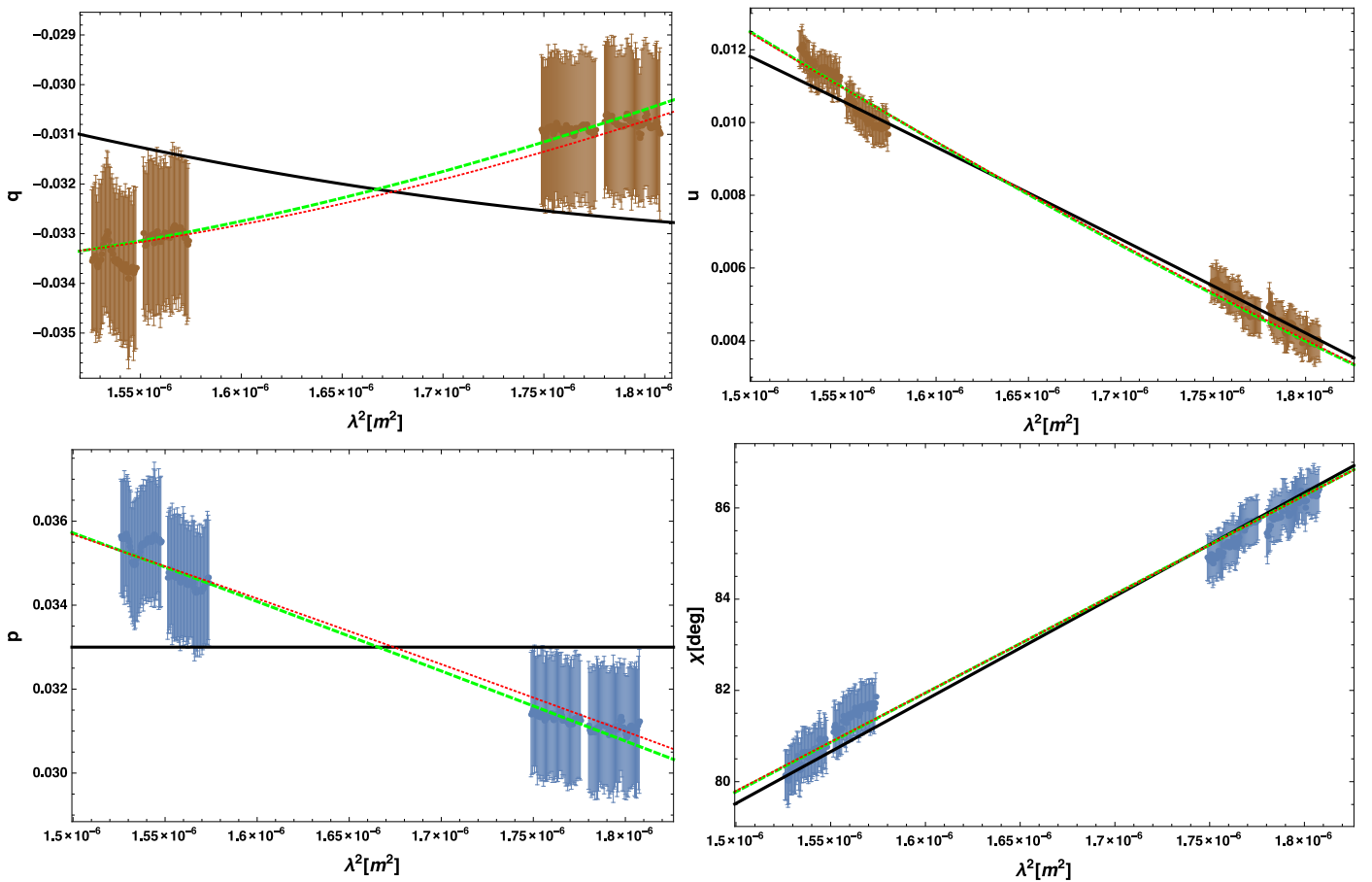


Fig. 3. Example fits from the qu-fitting overlaid on the data as a function of wavelength squared. Top left: Stokes Q/I. Top right: Stokes U/I. Bottom left: fractional polarization. Bottom right: EVPA. In all panels Model 1a (no depolarization) is shown by a black solid line, Model 1b (turbulent screen) is shown by a green dashed line, and Model 1c (ordered screen) is shown by a red dotted line.

of $6 \times 10^{-2} \text{cm}^{-3}$ found in the X-ray observations of Röser et al. (2000).

Alternatively, we can estimate the required magnetic field strength by assuming a value for the electron density. A higher electron density of 1000cm^{-3} , possibly typical of narrow line region clouds (Zavala & Taylor 2004), over a path length of 10 pc would result in a much smaller magnetic field strength of $44 \mu\text{G}$. In order to constrain this further, we need to compare our observation to simulations similar to those of Mościbrodzka et al. (2017), which we plan to do in a forthcoming publication.

The simplest models that can explain the depolarization across the band and the mean RM value are Faraday depolarization due to external Faraday dispersion or an RM gradient. External Faraday dispersion occurs when polarized emission passes through a Faraday screen with a Gaussian distribution of rotating cells covering the finite extent of the emission region. An unresolved RM gradient can also depolarize the emission in a similar manner due to the systematic RM variation across the emission region. The synthesized beam size of our observations is $0.8''$, which at the distance of 3C 273 translates to 2.1 kpc, and includes the entire parsec-scale jet as observed by VLBI.

Because of the limited wavelength coverage and angular resolution, our observations cannot distinguish between the cases where the depolarization is due to a turbulent magnetic field or an ordered RM gradient. A turbulent magnetic field around the jet is formed when the jet is launched via the standard and normal evolution (SANE; Narayan et al. 2012) accretion model. This model is typically applicable to low-efficiency jets and has

recently been used to interpret the Faraday rotation observations of M87 (Mościbrodzka et al. 2017). Such a field structure could explain the Faraday depolarization we observe. In this case the dispersion in the RM screen should be $\sim 2.7 \times 10^5 \text{rad m}^{-2}$ within the beam.

If the black hole is surrounded by dynamically important poloidal magnetic fields, a magnetically arrested disk (MAD; Tchekhovskoy et al. 2011) can form, efficiently launching jets. In this case, one would expect an ordered, helical magnetic field to surround the jet as the poloidal field is wound up into a tight helix due to the rotation of the black hole/accretion disk system (e.g., Meier et al. 2001). This model is supported by observations of a parsec-scale transverse Faraday rotation measure gradient in 3C 273 (e.g., Asada et al. 2002; Zavala & Taylor 2005; Hovatta et al. 2012); although this RM gradient is too small to cause the observed depolarization in our ALMA data. However, if this RM gradient is substantially larger in the inner jet region then it can explain the depolarization we observe. In particular, an RM gradient of $\sim 8.7 \times 10^5 \text{rad m}^{-2}$ across the beam is required. We plan to compare our observations directly with simulations in a forthcoming publication.

4.1. RM as a function of frequency

The behavior of RM as a function of frequency can tell us about the underlying conditions in the jet as both the electron density and magnetic field strength change as a function of distance from the black hole, which under certain assumptions can be trans-

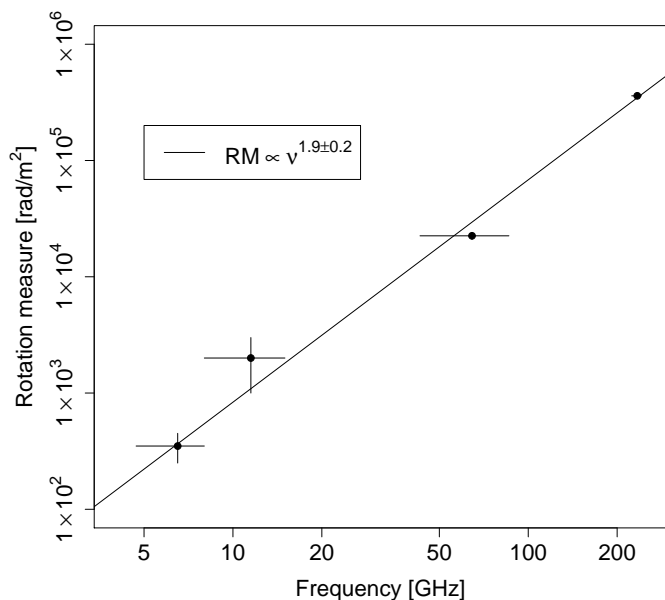


Fig. 4. Rotation measure as a function of frequency for 3C 273. The RM values at lower than ALMA 224 – 242 GHz frequency from this study are taken from the near-core region in VLBA observations from the literature (see text for references). Apart from the ALMA observation, the uncertainty in RM is a range of reported values, not an uncertainty in a single measurement. Similarly, the frequency range of the observations over the which the RM was estimated is shown by a solid line.

lated to observing frequency. As derived in Jorstad et al. (2007), in a conical jet under equipartition the RM is expected to follow a relation $|RM| \propto \nu^a$, where the value of a depends on the power-law change in the electron density n_e as a function of distance r from the black hole, $n_e \propto r^{-a}$. For example, $a = 2$ would imply that the Faraday rotation is occurring in a sheath around a conically expanding jet while smaller values could be explained with a more highly collimated jet (e.g., O’Sullivan & Gabuzda 2009). The typical values for a obtained in the literature vary in the range (0.9 – 4) with average or median values around 2 (Jorstad et al. 2007; O’Sullivan & Gabuzda 2009; Kravchenko et al. 2017).

In order to look for the frequency dependency in 3C 273, we gathered from the literature previously reported values for the core RM at different frequency ranges. As the core in 3C 273 at lower frequencies is typically depolarized, we have selected the value nearest to the core, so that these should formally be considered as lower limits. If multiple values are reported in the literature, we take their mean as the RM value and use the range as an uncertainty in the calculation of the slope. We used the range $RM = 250 - 450 \text{ rad m}^{-2}$ in the frequency range 4.7 – 8 GHz from Asada et al. (2002). This value is taken about 5 mas from the core and therefore is probably much lower than expected for the core. For the frequency range 8 – 15 GHz we use the range of near-core RM values of $RM = 1000 - 3000 \text{ rad m}^{-2}$ reported in Zavala & Taylor (2005) and Hovatta et al. (2012). For the 43 – 86 GHz range we use the range of lower limits $2.1 - 2.4 \times 10^4 \text{ rad m}^{-2}$ from Attridge et al. (2005) and Hada et al. (2016).

The linear fit to these data is shown in Fig. 4. We obtain $a = 1.9 \pm 0.2$, consistent with the mean value of $a = 1.8 \pm 0.2$ by Jorstad et al. (2007), and close to the expected value $a = 2$ for a sheath surrounding a conically expanding flow. However, this slope should be considered as an upper limit because the RM values at the lower frequencies are most certainly lower limits. Our

result is also consistent with the analysis presented in Plambeck et al. (2014), who found the extrapolation from lower frequencies with a slope of $a = 2$ to agree with their high RM of $9 \times 10^5 \text{ rad m}^{-2}$ detected at 1.3 mm in 3C 84.

At 1 mm wavelength, the emission in 3C 273 is already optically thin (e.g., Courvoisier 1998; Planck Collaboration et al. 2011) so that we may be viewing the polarized emission very close to the black hole. For example, in the models by Marscher (1980) and Potter & Cotter (2012), the emission at optically thin millimeter-band frequencies originates from the region where the jet transitions from a parabolic, magnetically dominated jet, to a conical jet in equipartition (referred to as the transition region later in the text). This is supported by simulations of Porth et al. (2011), who show that at higher, optically thin frequencies the polarized flux from the unresolved core (jet base in case of optically thin emission) begins to dominate the RM signal, which can reach values up to 10^6 rad m^{-2} , similar to what we detect.

However, it is also possible that the polarized emission is dominated by a single polarized jet component further down the jet as seen in a 86 GHz VLBI image of 3C 273 taken in May 2016 (Casadio et al. 2017). In their image, the core is depolarized, possibly due to opacity, because at 86 GHz, 3C 273 is in the transition to becoming optically thin. The image of Casadio et al. (2017) is taken 3 months after a peak of a large total flux density flare⁶, and the polarized component may be related to this flaring activity. The peak polarized flux density detected by Casadio et al. (2017) is about 200 mJy/beam. Assuming a spectral index of -0.75 , we would expect to see about 100 mJy of polarized flux in our 1 mm observations; instead, we observe a higher polarized flux density of about 150 mJy. Moreover, our observations are taken 7 months after the VLBI observations during a dip in the total flux density curve, and just before a new flare starts to rise. Perhaps it is more likely that we are seeing emission related to the new flaring activity, closer to the transition region.

One way to study this further is by investigating the behavior of the RM gradient as a function of frequency, assuming that the depolarization is due to an extension of the RM gradient seen on parsec scales. Wardle (2018) collected from the literature all the previous measurements of the RM gradient in 3C 273 and plotted them in their figure 5b. Because the RM is expected to follow a relation $|RM| \propto d^{-a}$, where d is the distance along the jet (Jorstad et al. 2007), we would expect the slope to be similar as obtained for the relation between the core RM and the frequency of observations. Indeed, Wardle (2018) finds a slope of -1.9 , consistent with our estimate from the mean RM value, supporting the interpretation that the RM is connected to the evolution of the electron density and magnetic field along the jet.

If at 1 mm wavelength we are seeing the optically thin emission in the jet transition region, observations at even higher frequencies should result in similar RM values as we have now obtained, assuming that the external Faraday screen is stable. Simultaneous observations at multiple frequencies will help to answer this question.

Our observed RM_{obs} of $3.6 \times 10^5 \text{ rad m}^{-2}$ corresponds to $RM_{\text{int}} = RM_{\text{obs}}(1+z)^2 = 4.8 \times 10^5 \text{ rad m}^{-2}$ in the frame of the source, at an emitted frequency of $\nu_{\text{em}} = \nu_{\text{obs}}(1+z) = 270 \text{ GHz}$ when using the central observed frequency $\nu_{\text{obs}} = 234 \text{ GHz}$. This is still much smaller than the intrinsic RM of 10^8 rad m^{-2} seen in the quasar PKS 1830–211 by Martí-Vidal et al. (2015). This

⁶ See the ALMA Calibrator Source Catalogue at <https://almascience.eso.org/sc/> for the total flux density evolution of the source.

could partially be explained with the higher redshift ($z = 2.5$) of PKS 1830–211, which makes the emitted frequency over which the RM was detected correspond to 875–1050 GHz, and which could possibly originate from closer to the black hole where the electron density and magnetic field is expected to be higher. If we estimate the expected RM at these high frequencies using the slope 1.9 from above, we obtain an intrinsic RM of $\sim 4 \times 10^6 \text{ rad m}^{-2}$, suggesting that the reason for the lower RM in 3C 273 is due to intrinsic differences in the electron density and/or magnetic field strength in these two sources. Studying a larger number of sources will allow us to establish if these type of differences are common between various AGN.

4.2. Possibility of multiple emission components

Because we do not spatially resolve the emission region with these ALMA observations, we have assumed that the polarization and RM signal are dominated by a single emission component. Although the recent VLBI observations by Casadio et al. (2017) support this assumption, it depends on the time of the observations because Hada et al. (2016) and Savolainen (in prep.) detect multiple polarized jet components in their earlier 86 GHz VLBI observations.

Our claimed detection of Faraday depolarization is dependent on our assumption that a single polarized component is dominating the emission (and that we have accurately characterized the calibration errors). If there is more than one brightly polarized component within the beam, then a two RM component model can also explain the observed polarization behavior (without the need for significant Faraday depolarization). For example, a model with $p_{01} \sim 5.7\%$, $p_{02} \sim 3.6\%$, $\text{RM}_1 \sim +2.6 \times 10^5 \text{ rad m}^{-2}$, $\text{RM}_2 \sim +1.8 \times 10^4 \text{ rad m}^{-2}$, $\chi_{01} \sim 76^\circ$, $\chi_{02} \sim 26^\circ$ can provide a similarly good fit to the observed data. However, due to the limited wavelength-squared coverage we do not claim that this fit is unique (i.e. other combinations of parameters for a two RM component model may also provide similar fits to the data).

Future Event Horizon Telescope (Doeleman et al. 2009) and Global Millimeter VLBI Array (GMVA) + ALMA (e.g., Boccardi et al. 2017) observations of 3C 273 should be able to spatially resolve the mm-emission region in 3C 273 and help determine the true origin and properties of this Faraday rotation medium.

4.3. Circular polarization

Although circular polarization observations are not yet officially offered by the ALMA Observatory, our Monte Carlo uncertainty assessment, described in Appendix A, allows us to investigate the Stokes V signal in our data. Assuming that we have accounted for all the possible errors in the data, we find that the instrumental contribution to the total Stokes V is about 2–3 mJy while there seems to be an intrinsic signal of about 10 mJy across the band (see Appendix A for details). This would indicate a fractional circular polarization of $\sim 0.2\%$. This result should be treated with caution, and we would need further ALMA observations (with properly supported circular polarimetry) to verify the detection. However, the value we obtain is consistent with the 1.3 mm circular polarization observations by the POLAMI group (Thum et al. 2018) who typically do not detect significant circular polarization from 3C 273, which is then expected as their uncertainties are typically higher than 0.2%.

Assuming a magnetic field strength of $\sim 6 \text{ G}$ in the region dominating the mm emission and a Doppler factor of ~ 5 (Savolainen et al. 2008), an intrinsic circular polarization as large as 1.8% can be obtained for a completely uniform jet magnetic field. Alternatively, if Faraday rotation-driven conversion is dominating the production of circular polarization, then the observed Stokes V level of $\sim 0.2\%$ could be obtained from 5% linear polarization with a low energy relativistic electron energy spectrum cut-off of ~ 4.5 (e.g., Homan et al. 2009; O’Sullivan et al. 2013). This would only provide an internal Faraday depth of order 10^5 of rad m^{-2} and thus indicates that the majority of the Faraday rotating material we detect is likely in a boundary layer or wind external to the jet.

5. Conclusions

We have studied the quasar 3C 273 at 1 mm wavelength with ALMA in full polarization mode at 0.8 mas resolution, corresponding to 2.1 kpc at the distance of 3C 273. We detect about 3.3% linear polarization in the unresolved core of the source, and model the polarization as a function of wavelength over the 1 mm band. Our main conclusions can be summarized as follows.

1. We detect a very high Faraday rotation measure (RM) of $(3.6 \pm 0.3) \times 10^5 \text{ rad m}^{-2}$ over the band implying a magnetic field of several Gauss or a high electron density of $\sim 1000 \text{ cm}^{-3}$ in the Faraday rotating medium probed by the polarized emission. This amount of Faraday rotation rotates the EVPAs in the 1 mm wavelength by over 30° , showing that it cannot be ignored when studying the intrinsic EVPA and magnetic field direction.
2. By modeling the Stokes parameters as a function of wavelength, we find that models with depolarization are strongly favored over no depolarization. Assuming that the polarized emission is dominated by a single region, we find that external Faraday dispersion or an RM gradient over the beam are able to explain our observations. Further multifrequency and high angular resolution observations are required to distinguish between the models.
3. Comparing the RM at 1 mm to values obtained at lower frequencies, we find the RM to increase as a function of observing frequency, following a power law with an index of $< 1.9 \pm 0.2$, consistent with a sheath surrounding a conically expanding jet.
4. Through careful Monte Carlo assessment of the systematic uncertainties in the polarization observations, we are able to detect about 0.2% of circular polarization. Further dedicated circular polarization observations are needed to confirm the result.

Acknowledgements. This paper makes use of the following ALMA data: ADS/JAO.ALMA#2016.1.01073.S. ALMA is a partnership of ESO (representing its member states), NSF (USA) and NINS (Japan), together with NRC (Canada), NSC and ASIAA (Taiwan), and KASI (Republic of Korea), in cooperation with the Republic of Chile. The Joint ALMA Observatory is operated by ESO, AUI/NRAO and NAOJ. This publication has received funding from the European Union’s Horizon 2020 research and innovation programme under grant agreement No 730562 [RadioNet]. TH was supported by the Turku Collegium of Science and Medicine. TS was funded by the Academy of Finland projects 274477 and 284495. AT was supported by the TAC fellowship.

References

- Anderson, C. S., Gaensler, B. M., & Feain, I. J. 2016, *ApJ*, 825, 59
 Asada, K., Inoue, M., Uchida, Y., et al. 2002, *PASJ*, 54, L39
 Attridge, J. M., Wardle, J. F. C., & Homan, D. C. 2005, *ApJ*, 633, L85

Blandford, R. D. & Znajek, R. L. 1977, MNRAS, 179, 433

Boccardi, B., Krichbaum, T. P., Ros, E., & Zensus, J. A. 2017, A&A Rev., 25, 4

Bower, G. C., Dexter, J., Markoff, S., Rao, R., & Plambeck, R. L. 2017, ApJ, 843, L31

Brentjens, M. A. & de Bruyn, A. G. 2005, A&A, 441, 1217

Broderick, A. E. & McKinney, J. C. 2010, ApJ, 725, 750

Burn, B. J. 1966, MNRAS, 133, 67

Casadio, C., Krichbaum, T., Marscher, A., et al. 2017, Galaxies, 5, 67

Courvoisier, T. J.-L. 1998, A&A Rev., 9, 1

De Villiers, J.-P., Hawley, J. F., Krolik, J. H., & Hirose, S. 2005, ApJ, 620, 878

Doeleman, S., Agol, E., Backer, D., et al. 2009, in , astro2010: The Astronomy and Astrophysics Decadal Survey, arXiv:0906.3899

Farnes, J. S., Gaensler, B. M., & Carretti, E. 2014, ApJS, 212, 15

Farnsworth, D., Rudnick, L., & Brown, S. 2011, AJ, 141, 191

Hada, K., Kino, M., Doi, A., et al. 2016, ApJ, 817, 131

Hawley, J. F. & Krolik, J. H. 2006, ApJ, 641, 103

Heald, G., Braun, R., & Edmonds, R. 2009, A&A, 503, 409

Homan, D. C., Lister, M. L., Aller, H. D., Aller, M. F., & Wardle, J. F. C. 2009, ApJ, 696, 328

Hovatta, T., Lister, M. L., Aller, M. F., et al. 2012, AJ, 144, 105

Jorstad, S. G., Marscher, A. P., Stevens, J. A., et al. 2007, AJ, 134, 799

Kravchenko, E. V., Kovalev, Y. Y., & Sokolovsky, K. V. 2017, MNRAS, 467, 83

Kuo, C. Y., Asada, K., Rao, R., et al. 2014, ApJ, 783, L33

Lobanov, A. P. 1998, A&AS, 132, 261

Marscher, A. P. 1980, ApJ, 235, 386

Martí-Vidal, I., Muller, S., Vlemmings, W., Horellou, C., & Aalto, S. 2015, Science, 348, 311

Martí-Vidal, I., Vlemmings, W. H. T., Muller, S., & Casey, S. 2014, A&A, 563, A136

McKinney, J. C. & Blandford, R. D. 2009, MNRAS, 394, L126

McKinney, J. C. & Gammie, C. F. 2004, ApJ, 611, 977

Meier, D. L., Koide, S., & Uchida, Y. 2001, Science, 291, 84

Mościbrodzka, M., Dexter, J., Davelaar, J., & Falcke, H. 2017, MNRAS, 468, 2214

Nagai, H., Nakanishi, K., Paladino, R., et al. 2016, ApJ, 824, 132

Narayan, R., Sądowski, A., Penna, R. F., & Kulkarni, A. K. 2012, MNRAS, 426, 3241

O’Sullivan, S. P., Brown, S., Robishaw, T., et al. 2012, MNRAS, 421, 3300

O’Sullivan, S. P. & Gabuzda, D. C. 2009, MNRAS, 393, 429

O’Sullivan, S. P., McClure-Griffiths, N. M., Feain, I. J., Gaensler, B. M., & Sault, R. J. 2013, MNRAS, 435, 311

O’Sullivan, S. P., Purcell, C. R., Anderson, C. S., et al. 2017, MNRAS, 469, 4034

Plambeck, R. L., Bower, G. C., Rao, R., et al. 2014, ApJ, 797, 66

Planck Collaboration, Aarokoski, J., Ade, P. A. R., et al. 2011, A&A, 536, A15

Porth, O., Fendt, C., Meliani, Z., & Vaidya, B. 2011, ApJ, 737, 42

Potter, W. J. & Cotter, G. 2012, MNRAS, 423, 756

Raftery, A. E. 1995, Sociological Methodology, 25, 111

Röser, H.-J., Meisenheimer, K., Neumann, M., Conway, R. G., & Perley, R. A. 2000, A&A, 360, 99

Savolainen, T., Wiik, K., Valtaoja, E., & Tornikoski, M. 2008, in Astronomical Society of the Pacific Conference Series, Vol. 386, Extragalactic Jets: Theory and Observation from Radio to Gamma Ray, ed. T. A. Rector & D. S. De Young, 451

Schnitzeler, D. H. F. M. 2018, MNRAS, 474, 300

Sokoloff, D. D., Bykov, A. A., Shukurov, A., et al. 1998, MNRAS, 299, 189

Strauss, M. A., Huchra, J. P., Davis, M., et al. 1992, ApJS, 83, 29

Taylor, G. B. 1998, ApJ, 506, 637

Tchekhovskoy, A., Narayan, R., & McKinney, J. C. 2011, MNRAS, 418, L79

Thum, C., Agudo, I., Molina, S. N., et al. 2018, MNRAS, 473, 2506

Vlemmings, W. H. T., Khouri, T., Martí-Vidal, I., et al. 2017, A&A, 603, A92

Wardle, J. 2018, Galaxies, 6, 5

Zavala, R. T. & Taylor, G. B. 2004, ApJ, 612, 749

Zavala, R. T. & Taylor, G. B. 2005, ApJ, 626, L73

Noise type	Noise mean	Noise std.
D-terms (real & imag)	0	1%
X-Y Phase	0	2 deg.
X-Y bandpass (amplitude)	0	0.1%
X-Y bandpass (phase)	0	0.5 deg.
Thermal (cont.)	0	1.3×10^{-5} Jy

Table A.1. Parameters of the (Gaussian) noise distributions used to perturb the ALMA data in our Monte Carlo polarimetry assessment. “X-Y Phase” is the residual phase between the polarizers at the reference antenna. “X-Y bandpass” is the (channel-wise) residual noise of the bandpass, relative between polarizers. “Thermal” is the theoretical image sensitivity in the continuum (as estimated from the ALMA Sensitivity Calculator). “D-terms” is the (channel-wise) residual polarization leakage.

Appendix A: Assessment of the Polarization Calibration

The accuracy of the ALMA polarimetry, which may be affected by an imperfect polarization calibration, has been assessed via a Monte Carlo analysis, following a procedure similar to that explained in Vlemmings et al. (2017) (see their Appendix A). These simulations are specifically designed to account for the systematic uncertainties arising from the polarization calibration.

In our Monte Carlo analysis, each gain contribution to the full calibration (i.e., bandpass, amplitude and phase gains, polarization leakage, amplitude ratio between polarizers, and phase spectrum between the polarizers at the reference antenna) was perturbed with random noise. For each realization of the noise, the complete set of Stokes parameters of the target was derived, by fitting a point source located at the phase center. This translated into a distribution of Stokes parameters, which reflect the posteriori probability density of the target parameters, as given from the assumed noise distribution of the antenna gains. The parameters of the gain-noise distributions are summarized in Table A.1. In addition to the noise added to the calibration tables, an extra contribution of thermal noise was added to each Stokes parameter at each iteration, to reflect the effects of the finite ALMA sensitivity.

The noise parameters given in Table A.1 are based on an educated guess, from our experience with ALMA polarimetry calibration (with the exception of the baseline sensitivity, which is taken from the theoretical thermal noise at ALMA, as estimated with the ALMA Sensitivity Calculator⁷). The gains of each spectral window were perturbed with independent gain noises, with the exception of the “X-Y phase” (which is fitted by CASA using the same polarization model for all spws).

Appendix A.1: Monte Carlo results I: linear polarization

We show in Fig. A.1 (blue) the distributions of the differences (averaged over all frequency channels) between the polarization properties derived from the Monte Carlo iterations and the polarization properties derived from the original ALMA calibration tables. The accuracy in the estimate of the fractional linear polarization (which we estimate from the dispersion of m differences) is very high, of the order of 0.02%. The gain-noise contribution to the polarization angle, ϕ , is of the order of $0.5\text{--}1^\circ$, with a slightly higher probability of rotating clockwise.

We have also computed the Rotation Measure (RM) from each Monte Carlo iteration. The distribution of RM devia-

⁷ <https://almascience.eso.org/proposing/sensitivity-calculator>

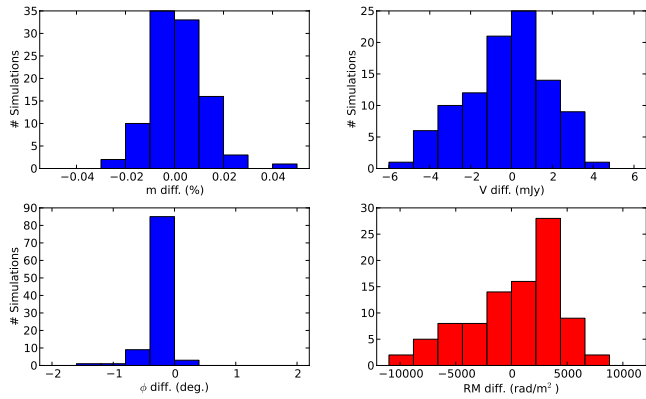


Fig. A.1. In blue, distributions of the difference between polarization properties from the Monte Carlo iterations and those derived from the original calibration. In red, difference in RM derived from a fit to the whole spectrum

tions with respect to the value estimated from the original calibration is shown in Fig. A.1 (red). The standard deviation is $\sim 4000 \text{ rad m}^{-2}$, with a slightly higher probability of biasing toward negative deviations.

Appendix A.2: Monte Carlo results II: circular polarization

The uncertainty in Stokes V , as estimated from Fig. A.1 (standard deviation of 2 mJy), is a large fraction of the total Stokes V derived from the original calibration (continuum average of ~ 10 mJy). This indicates that part of the detected V may be due to gain noise (in particular, to inaccuracies in the estimate of the cross-polarization phases at the reference antenna). However, we note that any spurious Stokes V caused by this kind of calibration errors would depend on the source parallactic angle, since the spurious V would be related to leakage from the linear polarization in the frame solidary to the antenna mounts. In particular, a calibration-related spurious circular polarization, V^{sp} , would be given by

$$V^{\text{sp}} \sim V^{\text{true}} \cos \Delta + (U \sin(\phi - \psi) + Q \cos(\phi - \psi)) \sin \Delta, \quad (\text{A.1})$$

where Δ is an instrumental phase offset between the X and Y polarizers at the reference antenna, ϕ is the EVPA of the source, ψ is the parallactic angle, V^{true} is the Stokes V intrinsic to the source, and U and Q are the other Stokes parameters intrinsic to the source (and in the sky frame).

In Fig. A.2, we show the Stokes V recovered from the original ALMA calibration (averaged over all the spectral channels) as a function of parallactic angle. A sinusoidal dependence of V is seen as a function of parallactic angle, which cannot be related to emission intrinsic to the source. This dependence can be explained as due to calibration artifacts (Eq. A.1), i.e. introduced by leakage from the linear polarization due to an error in the cross-polarization phase, Δ . Indeed, given that the average EVPA is $\sim 83^\circ$, we would expect the sinusoid to have a null close to a parallactic angle $\psi \sim (90 - 83)^\circ$ (according to Eq. A.1), as seems to be the case (Fig. A.2).

Using Eq. A.1, we estimate that the observed dependence of V with parallactic angle can be produced by a cross-polarization phase offset of $\Delta \sim 1^\circ$, given a fractional linear polarization of $\sim 3\%$. Indeed, the uncertainty level in Stokes V derived from our Monte Carlo simulations (Fig. A.1) is of the order of the amplitude in the sinusoid seen in the calibrated data (Fig. A.2), which

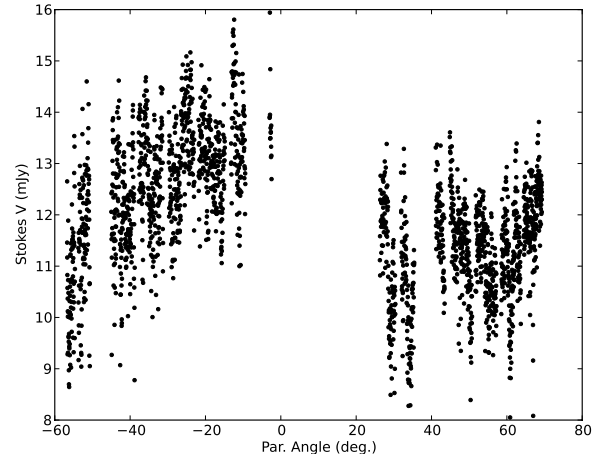


Fig. A.2. Frequency-averaged Stokes V , recovered from the original ALMA calibration, as a function of parallactic angle.

indicates that our Monte Carlo estimates of polarimetric uncertainties are realistic.

We notice, though, that there is another contribution to Stokes V (at a level of about 10 mJy) that is independent of the parallactic angle and may be related to intrinsic Stokes V from the source (i.e., V^{true} in Eq. A.1). This conclusion should, however, be taken with care. Circular polarization is still not officially supported by the ALMA observatory, and even though we do account for all the residual gain factors in our Monte Carlo analysis (see Table A.1), we would need further ALMA observations (with a properly supported circular polarimetry) for the re-assessment of these results.

In short, the conclusion from the assessment of the circular polarization is that there is evidence of spurious contribution from gain noise (via the dependence of V with parallactic angle), but also evidence of intrinsic Stokes V from the source. In any case, the low level of Stokes V , together with other contributions from the gain noise, make the flux-density estimate of such an intrinsic V component difficult.

Appendix A.2.1: Spectrum of Stokes V

In Fig. A.3, we show the Monte Carlo distribution of the spectral index of Stokes V (i.e., α , with $V \propto \nu^\alpha$). Accounting for residual leakage, residual bandpass (in amplitude and phase) and residual cross-polarization phases, the spectral index of Stokes V appears tightly bounded within positive values (i.e., inverted spectrum) around $\alpha \sim 0.6$. In other words, the frequency dependence of Stokes V is robust against the calibration uncertainties studies in our Monte Carlo analysis.

Nevertheless, and as we have noted in the previous section, there is evidence of an instrumental contribution (with an amplitude of about 2–3 mJy) to the measured Stokes V , which has an amplitude of ~ 12 mJy. Since the change in V across the spectral coverage of our ALMA observations is of the order of the instrumental effects, our conclusion about the V spectrum should also be treated with caution, and further observations would be needed to confirm this result.

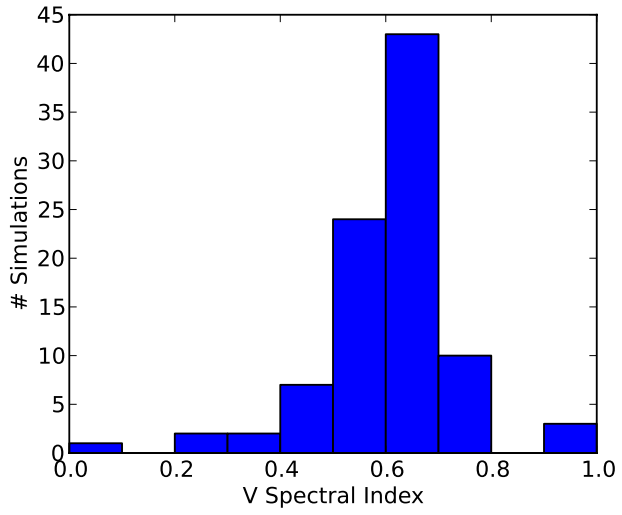


Fig. A.3. Monte Carlo distribution of the spectral index of Stokes V.

Table 1. Stokes parameters and the derived polarization fraction and EVPA for each spectral channel.

Freq. (GHz)	Stokes I (Jy)	Stokes Q (Jy)	Stokes U (Jy)	Stokes V (Jy)	Pol. fraction (%)	EVPA (°)
223.14	4.672±0.002	-0.145 ± 0.008	0.018±0.002	0.011±0.010	3.12±0.18	86.41±0.36
223.17	4.671±0.003	-0.145 ± 0.007	0.018±0.002	0.012±0.011	3.12±0.16	86.36±0.38
223.20	4.670±0.003	-0.144 ± 0.006	0.019±0.002	0.014±0.011	3.11±0.14	86.26±0.41
223.23	4.669±0.003	-0.144 ± 0.008	0.019±0.003	0.014±0.009	3.10±0.17	86.25±0.41
223.27	4.669±0.003	-0.143 ± 0.007	0.018±0.003	0.013±0.011	3.10±0.16	86.33±0.44
223.30	4.668±0.003	-0.144 ± 0.007	0.018±0.003	0.013±0.009	3.10±0.16	86.41±0.44
223.33	4.667±0.003	-0.144 ± 0.006	0.018±0.003	0.012±0.009	3.11±0.14	86.39±0.45
223.36	4.668±0.003	-0.144 ± 0.007	0.019±0.002	0.013±0.010	3.11±0.14	86.26±0.41
223.39	4.668±0.003	-0.144 ± 0.007	0.019±0.002	0.013±0.010	3.11±0.15	86.27±0.43
223.42	4.666±0.003	-0.144 ± 0.007	0.018±0.002	0.011±0.009	3.11±0.15	86.34±0.37
223.45	4.665±0.002	-0.144 ± 0.007	0.019±0.002	0.011±0.009	3.11±0.15	86.34±0.39
223.48	4.665±0.003	-0.144 ± 0.007	0.018±0.002	0.012±0.011	3.10±0.15	86.38±0.39
223.52	4.665±0.003	-0.143 ± 0.007	0.018±0.002	0.012±0.011	3.10±0.16	86.36±0.37
223.55	4.665±0.003	-0.143 ± 0.007	0.019±0.002	0.013±0.011	3.09±0.14	86.16±0.44
223.58	4.665±0.003	-0.142 ± 0.007	0.020±0.002	0.012±0.009	3.08±0.15	86.00±0.48
223.61	4.664±0.003	-0.143 ± 0.007	0.019±0.002	0.011±0.011	3.09±0.15	86.14±0.40
223.64	4.663±0.003	-0.144 ± 0.008	0.019±0.002	0.011±0.009	3.11±0.17	86.22±0.38
223.67	4.663±0.003	-0.144 ± 0.007	0.019±0.002	0.011±0.010	3.11±0.15	86.16±0.40
223.70	4.663±0.003	-0.144 ± 0.007	0.019±0.003	0.010±0.010	3.11±0.16	86.25±0.46
223.73	4.662±0.003	-0.145 ± 0.006	0.018±0.002	0.010±0.010	3.12±0.14	86.38±0.42
223.77	4.663±0.003	-0.145 ± 0.006	0.019±0.003	0.011±0.010	3.13±0.13	86.25±0.47
223.80	4.663±0.003	-0.144 ± 0.007	0.020±0.003	0.011±0.010	3.13±0.15	86.11±0.43
223.83	4.663±0.003	-0.144 ± 0.006	0.020±0.002	0.012±0.010	3.11±0.14	86.14±0.41
223.86	4.661±0.003	-0.143 ± 0.007	0.019±0.002	0.011±0.010	3.10±0.15	86.15±0.40
223.89	4.660±0.003	-0.143 ± 0.008	0.019±0.002	0.010±0.010	3.10±0.16	86.19±0.40
223.92	4.658±0.003	-0.143 ± 0.006	0.020±0.003	0.011±0.010	3.11±0.13	86.12±0.45
223.95	4.657±0.003	-0.143 ± 0.007	0.020±0.003	0.011±0.009	3.11±0.15	85.99±0.42
223.98	4.657±0.003	-0.143 ± 0.007	0.020±0.003	0.010±0.011	3.11±0.15	86.04±0.44
224.02	4.657±0.003	-0.143 ± 0.008	0.020±0.003	0.011±0.010	3.11±0.18	86.01±0.40
224.05	4.657±0.003	-0.143 ± 0.007	0.021±0.002	0.013±0.009	3.10±0.15	85.89±0.43
224.08	4.656±0.003	-0.143 ± 0.007	0.021±0.002	0.013±0.011	3.11±0.15	85.87±0.39
224.11	4.656±0.003	-0.143 ± 0.007	0.021±0.002	0.013±0.010	3.10±0.15	85.83±0.42
224.14	4.655±0.003	-0.142 ± 0.007	0.021±0.002	0.013±0.010	3.09±0.16	85.82±0.41
224.17	4.655±0.003	-0.142 ± 0.007	0.020±0.003	0.012±0.010	3.09±0.15	85.91±0.41
224.20	4.654±0.003	-0.143 ± 0.007	0.020±0.003	0.010±0.010	3.10±0.15	86.01±0.39
224.23	4.652±0.003	-0.143 ± 0.007	0.020±0.003	0.011±0.010	3.11±0.15	86.09±0.46
224.27	4.651±0.003	-0.143 ± 0.007	0.020±0.002	0.012±0.010	3.11±0.15	86.11±0.39
224.30	4.651±0.003	-0.143 ± 0.007	0.020±0.002	0.012±0.010	3.11±0.14	86.13±0.42
224.33	4.651±0.003	-0.143 ± 0.008	0.020±0.003	0.012±0.012	3.11±0.17	86.08±0.43
224.36	4.650±0.003	-0.143 ± 0.007	0.021±0.002	0.013±0.010	3.11±0.16	85.91±0.38
224.39	4.650±0.003	-0.143 ± 0.007	0.021±0.003	0.014±0.011	3.11±0.15	85.80±0.42
224.42	4.649±0.002	-0.143 ± 0.007	0.021±0.002	0.012±0.012	3.11±0.14	85.78±0.38
224.45	4.648±0.003	-0.143 ± 0.007	0.021±0.002	0.012±0.009	3.12±0.15	85.81±0.41
224.48	4.648±0.003	-0.143 ± 0.006	0.021±0.002	0.013±0.010	3.11±0.14	85.80±0.40
224.52	4.649±0.003	-0.143 ± 0.007	0.021±0.002	0.011±0.010	3.11±0.15	85.77±0.38
224.55	4.648±0.003	-0.143 ± 0.008	0.021±0.003	0.010±0.011	3.10±0.17	85.81±0.40
224.58	4.646±0.003	-0.143 ± 0.008	0.021±0.003	0.010±0.010	3.11±0.17	85.85±0.42
224.61	4.645±0.003	-0.143 ± 0.007	0.021±0.003	0.012±0.009	3.10±0.15	85.76±0.43
224.64	4.645±0.003	-0.142 ± 0.008	0.021±0.002	0.014±0.010	3.10±0.16	85.74±0.41
224.67	4.644±0.003	-0.142 ± 0.007	0.021±0.002	0.014±0.010	3.10±0.15	85.86±0.40
224.70	4.644±0.003	-0.143 ± 0.007	0.021±0.002	0.013±0.009	3.10±0.16	85.77±0.39
224.73	4.644±0.003	-0.142 ± 0.007	0.022±0.003	0.012±0.010	3.10±0.16	85.61±0.44
224.77	4.643±0.003	-0.142 ± 0.007	0.022±0.003	0.012±0.011	3.10±0.16	85.61±0.42
224.80	4.643±0.003	-0.142 ± 0.007	0.022±0.002	0.013±0.011	3.10±0.15	85.52±0.42
224.83	4.643±0.003	-0.142 ± 0.007	0.023±0.003	0.014±0.011	3.10±0.15	85.38±0.49
224.86	4.642±0.003	-0.143 ± 0.007	0.023±0.002	0.014±0.010	3.11±0.16	85.45±0.40
225.14	4.644±0.002	-0.144 ± 0.007	0.022±0.002	0.011±0.011	3.13±0.14	85.74±0.37
225.17	4.644±0.003	-0.144 ± 0.007	0.021±0.003	0.012±0.011	3.13±0.15	85.77±0.39
225.20	4.643±0.003	-0.144 ± 0.007	0.022±0.002	0.013±0.010	3.14±0.15	85.75±0.37

Table 1. continued.

Freq. (GHz)	Stokes I (Jy)	Stokes Q (Jy)	Stokes U (Jy)	Stokes V (Jy)	Pol. fraction (%)	EVPA (°)
225.23	4.642±0.002	-0.144 ± 0.007	0.022±0.002	0.013±0.011	3.13±0.15	85.68±0.35
225.27	4.642±0.002	-0.144 ± 0.007	0.022±0.002	0.013±0.010	3.13±0.15	85.68±0.33
225.30	4.641±0.002	-0.144 ± 0.008	0.022±0.002	0.012±0.010	3.13±0.17	85.69±0.35
225.33	4.640±0.003	-0.144 ± 0.007	0.022±0.002	0.012±0.010	3.13±0.16	85.69±0.33
225.36	4.639±0.003	-0.144 ± 0.007	0.022±0.002	0.012±0.010	3.13±0.16	85.72±0.37
225.39	4.638±0.003	-0.143 ± 0.007	0.022±0.002	0.012±0.011	3.12±0.15	85.70±0.36
225.42	4.638±0.002	-0.143 ± 0.006	0.022±0.002	0.012±0.009	3.12±0.14	85.65±0.36
225.45	4.639±0.003	-0.143 ± 0.007	0.022±0.002	0.011±0.010	3.12±0.16	85.64±0.39
225.48	4.638±0.003	-0.143 ± 0.007	0.022±0.002	0.010±0.010	3.12±0.15	85.71±0.41
225.52	4.637±0.003	-0.143 ± 0.007	0.022±0.002	0.011±0.010	3.12±0.14	85.71±0.41
225.55	4.637±0.002	-0.143 ± 0.007	0.022±0.002	0.012±0.010	3.12±0.15	85.67±0.38
225.58	4.637±0.003	-0.143 ± 0.008	0.022±0.002	0.013±0.009	3.12±0.17	85.57±0.40
225.61	4.636±0.002	-0.143 ± 0.007	0.023±0.002	0.013±0.010	3.12±0.16	85.50±0.35
225.64	4.636±0.002	-0.143 ± 0.007	0.022±0.002	0.011±0.012	3.13±0.16	85.56±0.39
225.67	4.636±0.002	-0.143 ± 0.007	0.022±0.002	0.010±0.010	3.12±0.15	85.58±0.34
225.70	4.636±0.003	-0.143 ± 0.006	0.022±0.002	0.010±0.010	3.12±0.13	85.60±0.42
225.73	4.635±0.003	-0.143 ± 0.006	0.022±0.002	0.012±0.010	3.12±0.14	85.64±0.35
225.77	4.634±0.003	-0.143 ± 0.006	0.022±0.002	0.012±0.010	3.12±0.13	85.55±0.38
225.80	4.634±0.002	-0.143 ± 0.007	0.023±0.002	0.011±0.011	3.14±0.15	85.36±0.32
225.83	4.633±0.002	-0.144 ± 0.007	0.024±0.002	0.011±0.010	3.15±0.14	85.26±0.37
225.86	4.633±0.003	-0.144 ± 0.006	0.024±0.002	0.011±0.010	3.14±0.14	85.25±0.37
225.89	4.633±0.003	-0.143 ± 0.007	0.024±0.002	0.012±0.011	3.14±0.15	85.16±0.40
225.92	4.632±0.003	-0.143 ± 0.007	0.024±0.002	0.011±0.011	3.13±0.16	85.14±0.35
225.95	4.631±0.003	-0.143 ± 0.007	0.024±0.002	0.010±0.009	3.14±0.16	85.30±0.38
225.98	4.630±0.003	-0.144 ± 0.007	0.023±0.003	0.010±0.010	3.14±0.15	85.35±0.37
226.02	4.630±0.003	-0.143 ± 0.007	0.024±0.003	0.009±0.009	3.14±0.16	85.28±0.36
226.05	4.629±0.003	-0.143 ± 0.007	0.024±0.002	0.010±0.011	3.13±0.15	85.23±0.38
226.08	4.628±0.003	-0.143 ± 0.007	0.024±0.002	0.011±0.010	3.13±0.15	85.16±0.36
226.11	4.628±0.003	-0.143 ± 0.007	0.025±0.002	0.011±0.010	3.13±0.16	85.13±0.40
226.14	4.628±0.002	-0.143 ± 0.006	0.024±0.002	0.011±0.010	3.14±0.14	85.20±0.34
226.17	4.628±0.002	-0.143 ± 0.007	0.024±0.002	0.012±0.011	3.14±0.16	85.25±0.31
226.20	4.627±0.002	-0.143 ± 0.006	0.024±0.002	0.012±0.010	3.14±0.14	85.22±0.37
226.23	4.626±0.003	-0.143 ± 0.007	0.024±0.002	0.012±0.010	3.13±0.15	85.15±0.36
226.27	4.626±0.002	-0.143 ± 0.007	0.024±0.002	0.012±0.011	3.13±0.14	85.19±0.36
226.30	4.625±0.002	-0.143 ± 0.007	0.024±0.002	0.012±0.011	3.13±0.16	85.17±0.36
226.33	4.625±0.003	-0.143 ± 0.007	0.025±0.002	0.012±0.010	3.14±0.16	85.01±0.40
226.36	4.625±0.002	-0.142 ± 0.007	0.025±0.002	0.012±0.010	3.13±0.16	84.93±0.34
226.39	4.624±0.003	-0.142 ± 0.006	0.025±0.002	0.011±0.011	3.12±0.14	84.96±0.40
226.42	4.623±0.002	-0.143 ± 0.008	0.025±0.002	0.011±0.012	3.13±0.17	84.98±0.33
226.45	4.622±0.003	-0.143 ± 0.008	0.025±0.002	0.011±0.009	3.14±0.17	85.02±0.40
226.48	4.621±0.003	-0.143 ± 0.007	0.025±0.002	0.012±0.012	3.15±0.16	85.06±0.36
226.52	4.621±0.003	-0.143 ± 0.007	0.025±0.003	0.014±0.010	3.14±0.16	84.97±0.42
226.55	4.620±0.003	-0.142 ± 0.007	0.026±0.002	0.014±0.009	3.13±0.15	84.89±0.36
226.58	4.620±0.003	-0.143 ± 0.007	0.025±0.002	0.013±0.011	3.13±0.15	84.93±0.41
226.61	4.620±0.002	-0.143 ± 0.007	0.025±0.002	0.012±0.009	3.14±0.14	84.96±0.35
226.64	4.619±0.003	-0.142 ± 0.008	0.026±0.003	0.012±0.009	3.13±0.17	84.87±0.39
226.67	4.618±0.003	-0.143 ± 0.006	0.026±0.002	0.014±0.010	3.14±0.14	84.78±0.42
226.70	4.618±0.002	-0.143 ± 0.006	0.026±0.002	0.014±0.011	3.15±0.14	84.87±0.38
226.73	4.618±0.002	-0.143 ± 0.007	0.025±0.002	0.013±0.010	3.15±0.16	84.99±0.34
226.77	4.617±0.002	-0.143 ± 0.006	0.026±0.002	0.013±0.010	3.15±0.14	84.92±0.33
226.80	4.617±0.002	-0.143 ± 0.007	0.026±0.002	0.013±0.009	3.15±0.15	84.84±0.36
226.83	4.617±0.002	-0.143 ± 0.007	0.026±0.002	0.014±0.009	3.14±0.15	84.90±0.36
226.86	4.616±0.002	-0.143 ± 0.007	0.026±0.002	0.014±0.011	3.14±0.15	84.92±0.37
239.14	4.440±0.002	-0.147 ± 0.007	0.043±0.002	0.011±0.010	3.45±0.16	81.86±0.31
239.17	4.439±0.003	-0.147 ± 0.007	0.044±0.002	0.013±0.010	3.47±0.16	81.72±0.35
239.20	4.439±0.003	-0.147 ± 0.007	0.044±0.002	0.014±0.008	3.47±0.17	81.61±0.39
239.23	4.438±0.002	-0.147 ± 0.007	0.044±0.002	0.012±0.011	3.46±0.16	81.60±0.32
239.27	4.438±0.003	-0.147 ± 0.007	0.044±0.002	0.011±0.009	3.45±0.16	81.70±0.36
239.30	4.438±0.002	-0.147 ± 0.007	0.044±0.002	0.011±0.010	3.45±0.16	81.72±0.37
239.33	4.438±0.002	-0.146 ± 0.006	0.044±0.002	0.011±0.011	3.45±0.15	81.62±0.36

Table 1. continued.

Freq. (GHz)	Stokes I (Jy)	Stokes Q (Jy)	Stokes U (Jy)	Stokes V (Jy)	Pol. fraction (%)	EVPA (°)
239.36	4.438±0.002	-0.146 ± 0.007	0.044±0.002	0.011±0.009	3.44±0.15	81.58±0.36
239.39	4.438±0.002	-0.146 ± 0.007	0.044±0.002	0.012±0.009	3.44±0.15	81.70±0.38
239.42	4.437±0.002	-0.146 ± 0.007	0.044±0.002	0.011±0.011	3.44±0.16	81.71±0.37
239.45	4.437±0.002	-0.146 ± 0.006	0.044±0.002	0.010±0.010	3.43±0.14	81.64±0.35
239.48	4.436±0.002	-0.146 ± 0.006	0.044±0.002	0.011±0.008	3.43±0.14	81.65±0.39
239.52	4.435±0.002	-0.146 ± 0.007	0.044±0.002	0.012±0.010	3.44±0.17	81.68±0.34
239.55	4.435±0.003	-0.146 ± 0.006	0.044±0.002	0.013±0.010	3.44±0.14	81.61±0.35
239.58	4.435±0.003	-0.146 ± 0.006	0.044±0.002	0.012±0.010	3.44±0.14	81.60±0.36
239.61	4.435±0.002	-0.146 ± 0.007	0.044±0.002	0.011±0.009	3.44±0.16	81.66±0.36
239.64	4.435±0.002	-0.146 ± 0.006	0.044±0.002	0.011±0.010	3.43±0.15	81.60±0.32
239.67	4.435±0.003	-0.146 ± 0.007	0.044±0.002	0.012±0.010	3.43±0.16	81.60±0.36
239.70	4.433±0.002	-0.146 ± 0.006	0.044±0.002	0.013±0.010	3.43±0.14	81.65±0.35
239.73	4.432±0.002	-0.146 ± 0.008	0.044±0.002	0.012±0.010	3.43±0.18	81.66±0.32
239.77	4.432±0.002	-0.146 ± 0.007	0.044±0.002	0.012±0.010	3.44±0.17	81.60±0.29
239.80	4.431±0.002	-0.146 ± 0.007	0.045±0.002	0.012±0.009	3.45±0.16	81.50±0.33
239.83	4.430±0.003	-0.146 ± 0.007	0.045±0.002	0.012±0.010	3.46±0.16	81.44±0.38
239.86	4.430±0.003	-0.147 ± 0.006	0.045±0.002	0.011±0.011	3.46±0.14	81.48±0.38
239.89	4.430±0.002	-0.146 ± 0.006	0.045±0.002	0.012±0.010	3.46±0.14	81.48±0.34
239.92	4.430±0.002	-0.146 ± 0.006	0.045±0.002	0.012±0.010	3.45±0.13	81.46±0.34
239.95	4.430±0.003	-0.146 ± 0.006	0.044±0.002	0.012±0.008	3.45±0.14	81.58±0.40
239.98	4.429±0.002	-0.146 ± 0.007	0.044±0.002	0.012±0.009	3.45±0.15	81.62±0.32
240.02	4.428±0.003	-0.146 ± 0.007	0.044±0.002	0.011±0.010	3.45±0.16	81.54±0.37
240.05	4.427±0.002	-0.146 ± 0.006	0.045±0.002	0.012±0.010	3.45±0.14	81.50±0.33
240.08	4.427±0.002	-0.146 ± 0.007	0.045±0.002	0.013±0.010	3.45±0.16	81.50±0.30
240.11	4.426±0.003	-0.146 ± 0.006	0.045±0.002	0.013±0.010	3.46±0.14	81.48±0.37
240.14	4.426±0.002	-0.146 ± 0.006	0.045±0.002	0.012±0.009	3.46±0.15	81.43±0.33
240.17	4.426±0.003	-0.147 ± 0.007	0.045±0.002	0.012±0.009	3.47±0.16	81.40±0.41
240.20	4.426±0.002	-0.147 ± 0.008	0.045±0.002	0.011±0.010	3.47±0.17	81.47±0.39
240.23	4.426±0.002	-0.147 ± 0.006	0.045±0.002	0.012±0.009	3.47±0.15	81.48±0.38
240.27	4.426±0.003	-0.146 ± 0.007	0.045±0.002	0.013±0.010	3.46±0.15	81.42±0.37
240.30	4.425±0.002	-0.146 ± 0.006	0.045±0.002	0.013±0.010	3.46±0.14	81.39±0.31
240.33	4.424±0.002	-0.146 ± 0.007	0.046±0.003	0.013±0.010	3.45±0.17	81.28±0.34
240.36	4.423±0.002	-0.146 ± 0.007	0.046±0.002	0.013±0.010	3.46±0.16	81.29±0.34
240.39	4.422±0.002	-0.146 ± 0.007	0.046±0.002	0.014±0.010	3.46±0.16	81.33±0.33
240.42	4.422±0.002	-0.147 ± 0.007	0.046±0.002	0.013±0.011	3.47±0.15	81.34±0.35
240.45	4.422±0.002	-0.147 ± 0.007	0.045±0.002	0.012±0.010	3.47±0.17	81.44±0.35
240.48	4.421±0.002	-0.146 ± 0.007	0.046±0.002	0.012±0.009	3.47±0.16	81.33±0.34
240.52	4.421±0.002	-0.146 ± 0.007	0.047±0.002	0.012±0.010	3.46±0.16	81.16±0.33
240.55	4.420±0.002	-0.146 ± 0.007	0.047±0.002	0.013±0.009	3.47±0.16	81.16±0.34
240.58	4.419±0.002	-0.146 ± 0.007	0.047±0.002	0.014±0.010	3.47±0.17	81.14±0.35
240.61	4.418±0.002	-0.146 ± 0.007	0.047±0.002	0.013±0.010	3.47±0.16	81.15±0.30
240.64	4.417±0.003	-0.146 ± 0.007	0.047±0.003	0.012±0.010	3.47±0.16	81.15±0.38
240.67	4.418±0.002	-0.146 ± 0.008	0.047±0.002	0.012±0.010	3.47±0.18	81.09±0.38
240.70	4.418±0.002	-0.146 ± 0.006	0.047±0.002	0.013±0.009	3.48±0.14	81.03±0.30
240.73	4.417±0.002	-0.146 ± 0.007	0.047±0.002	0.015±0.008	3.48±0.16	81.04±0.37
240.77	4.416±0.002	-0.147 ± 0.006	0.047±0.002	0.016±0.011	3.49±0.15	81.19±0.34
240.80	4.415±0.002	-0.147 ± 0.007	0.046±0.002	0.015±0.010	3.49±0.15	81.25±0.36
240.83	4.415±0.002	-0.146 ± 0.007	0.046±0.002	0.014±0.010	3.48±0.15	81.20±0.33
240.86	4.413±0.002	-0.146 ± 0.007	0.047±0.002	0.015±0.010	3.47±0.16	81.09±0.33
241.14	4.403±0.002	-0.148 ± 0.007	0.050±0.002	0.014±0.010	3.55±0.17	80.76±0.36
241.17	4.403±0.003	-0.148 ± 0.007	0.049±0.002	0.016±0.009	3.55±0.16	80.84±0.37
241.20	4.403±0.002	-0.149 ± 0.007	0.049±0.002	0.015±0.010	3.55±0.16	80.94±0.35
241.23	4.402±0.003	-0.149 ± 0.008	0.049±0.002	0.013±0.010	3.56±0.18	80.91±0.40
241.27	4.401±0.002	-0.148 ± 0.006	0.050±0.002	0.012±0.010	3.56±0.13	80.76±0.34
241.30	4.400±0.002	-0.148 ± 0.007	0.050±0.002	0.013±0.008	3.55±0.15	80.64±0.32
241.33	4.400±0.002	-0.148 ± 0.006	0.050±0.002	0.014±0.010	3.56±0.14	80.68±0.34
241.36	4.400±0.002	-0.148 ± 0.007	0.050±0.002	0.013±0.010	3.56±0.15	80.75±0.35
241.39	4.399±0.002	-0.149 ± 0.007	0.049±0.002	0.013±0.009	3.56±0.17	80.81±0.33
241.42	4.398±0.002	-0.149 ± 0.008	0.049±0.002	0.014±0.011	3.57±0.18	80.95±0.33
241.45	4.398±0.003	-0.149 ± 0.007	0.049±0.002	0.014±0.010	3.57±0.17	80.91±0.35

Table 1. continued.

Freq. (GHz)	Stokes I (Jy)	Stokes Q (Jy)	Stokes U (Jy)	Stokes V (Jy)	Pol. fraction (%)	EVPA (°)
241.48	4.398±0.002	-0.149 ± 0.007	0.050±0.002	0.014±0.009	3.56±0.15	80.76±0.34
241.52	4.397±0.002	-0.148 ± 0.006	0.050±0.002	0.014±0.009	3.56±0.15	80.64±0.30
241.55	4.397±0.002	-0.148 ± 0.007	0.050±0.002	0.015±0.010	3.55±0.16	80.60±0.34
241.58	4.397±0.003	-0.148 ± 0.007	0.050±0.002	0.015±0.010	3.55±0.15	80.70±0.40
241.61	4.397±0.002	-0.148 ± 0.007	0.050±0.002	0.015±0.009	3.56±0.15	80.73±0.34
241.64	4.396±0.002	-0.148 ± 0.007	0.050±0.002	0.015±0.010	3.56±0.16	80.71±0.37
241.67	4.394±0.002	-0.148 ± 0.006	0.050±0.002	0.016±0.010	3.56±0.15	80.71±0.37
241.70	4.394±0.002	-0.148 ± 0.007	0.050±0.002	0.016±0.010	3.56±0.16	80.64±0.32
241.73	4.394±0.002	-0.148 ± 0.006	0.051±0.002	0.016±0.011	3.56±0.15	80.57±0.37
241.77	4.394±0.002	-0.148 ± 0.007	0.051±0.002	0.015±0.010	3.55±0.16	80.54±0.34
241.80	4.394±0.002	-0.147 ± 0.006	0.051±0.002	0.014±0.011	3.55±0.15	80.52±0.31
241.83	4.394±0.003	-0.148 ± 0.006	0.050±0.002	0.014±0.010	3.55±0.14	80.63±0.37
241.86	4.392±0.003	-0.148 ± 0.006	0.050±0.002	0.013±0.010	3.55±0.13	80.66±0.40
241.89	4.392±0.002	-0.147 ± 0.007	0.050±0.002	0.013±0.010	3.54±0.17	80.56±0.37
241.92	4.391±0.002	-0.147 ± 0.007	0.051±0.002	0.012±0.009	3.54±0.15	80.52±0.31
241.95	4.391±0.002	-0.147 ± 0.006	0.050±0.002	0.013±0.010	3.55±0.14	80.57±0.34
241.98	4.392±0.002	-0.147 ± 0.006	0.050±0.002	0.016±0.010	3.54±0.15	80.62±0.32
242.02	4.392±0.002	-0.147 ± 0.007	0.050±0.002	0.018±0.010	3.54±0.16	80.65±0.31
242.05	4.392±0.002	-0.147 ± 0.007	0.050±0.002	0.016±0.010	3.53±0.15	80.65±0.35
242.08	4.391±0.002	-0.146 ± 0.007	0.050±0.003	0.015±0.010	3.52±0.15	80.58±0.38
242.11	4.390±0.002	-0.146 ± 0.006	0.050±0.002	0.015±0.010	3.52±0.15	80.62±0.32
242.14	4.390±0.002	-0.146 ± 0.007	0.050±0.002	0.015±0.009	3.52±0.17	80.65±0.36
242.17	4.390±0.002	-0.146 ± 0.007	0.050±0.002	0.014±0.010	3.52±0.16	80.54±0.35
242.20	4.389±0.003	-0.145 ± 0.007	0.051±0.002	0.015±0.009	3.51±0.16	80.38±0.39
242.23	4.389±0.002	-0.145 ± 0.007	0.051±0.002	0.015±0.009	3.50±0.17	80.25±0.34
242.27	4.390±0.002	-0.145 ± 0.007	0.051±0.002	0.015±0.008	3.50±0.16	80.25±0.40
242.30	4.391±0.002	-0.145 ± 0.007	0.051±0.002	0.015±0.011	3.50±0.16	80.38±0.39
242.33	4.390±0.002	-0.145 ± 0.006	0.050±0.002	0.014±0.011	3.50±0.14	80.55±0.38
242.36	4.390±0.002	-0.145 ± 0.007	0.050±0.002	0.015±0.010	3.50±0.15	80.56±0.34
242.39	4.388±0.002	-0.145 ± 0.006	0.050±0.002	0.016±0.009	3.50±0.14	80.47±0.35
242.42	4.386±0.002	-0.146 ± 0.007	0.051±0.002	0.016±0.010	3.52±0.16	80.33±0.34
242.45	4.384±0.002	-0.146 ± 0.007	0.051±0.002	0.014±0.008	3.53±0.16	80.29±0.31
242.48	4.384±0.003	-0.146 ± 0.007	0.051±0.002	0.015±0.009	3.54±0.15	80.36±0.37
242.52	4.383±0.002	-0.147 ± 0.007	0.051±0.002	0.016±0.011	3.55±0.15	80.36±0.33
242.55	4.382±0.002	-0.147 ± 0.007	0.052±0.002	0.016±0.010	3.56±0.15	80.30±0.38
242.58	4.382±0.002	-0.147 ± 0.007	0.052±0.002	0.017±0.011	3.56±0.16	80.26±0.48
242.61	4.381±0.002	-0.147 ± 0.007	0.052±0.002	0.016±0.009	3.56±0.15	80.24±0.36
242.64	4.380±0.002	-0.148 ± 0.006	0.052±0.002	0.016±0.010	3.57±0.13	80.30±0.34
242.67	4.379±0.003	-0.147 ± 0.006	0.052±0.002	0.016±0.010	3.57±0.14	80.26±0.36
242.70	4.379±0.002	-0.147 ± 0.007	0.053±0.002	0.017±0.010	3.56±0.17	80.10±0.32
242.73	4.379±0.002	-0.146 ± 0.006	0.053±0.002	0.017±0.010	3.56±0.15	80.02±0.38
242.77	4.378±0.002	-0.147 ± 0.006	0.053±0.002	0.015±0.009	3.56±0.15	80.08±0.34
242.80	4.377±0.002	-0.147 ± 0.006	0.052±0.002	0.015±0.010	3.56±0.15	80.15±0.35
242.83	4.377±0.002	-0.147 ± 0.006	0.053±0.002	0.016±0.009	3.56±0.15	80.15±0.37
242.86	4.377±0.002	-0.147 ± 0.006	0.053±0.002	0.017±0.010	3.56±0.15	80.14±0.32